Kinetic model of C/H/N/O emissions in laser-induced breakdown spectroscopy of organic compounds

Paul J. Dagdigian,[1,*] Ani Khachatrian,[1] and Valeri I. Babushok[2]

[1]Department of Chemistry, The Johns Hopkins University, Baltimore Maryland 21218-2685, USA

[2]National Institutes of Standards and Technology, Gaithersburg, Maryland 20899, USA

*Corresponding author: pjdagdigian@jhu.edu

Received 18 September 2009; revised 12 January 2010; accepted 15 January 2010; posted 21 January 2010 (Doc. ID 117220); published 24 February 2010

A kinetic model to predict the relative intensities of the atomic C/H/N/O emission lines in laser-induced breakdown spectroscopy (LIBS) has been developed for organic compounds. The model includes a comprehensive set of chemical processes involving both neutral and ionic chemistry and physical excitation and de-excitation of atomic levels affecting the neutral, ionic, and excited-state species concentrations. The relative excited-state atom concentrations predicted by this modeling are compared with those derived from the observed LIBS intensities for 355 nm ns laser irradiation of residues of two organic compounds on aluminum substrate. The model reasonably predicts the relative excited-state concentrations, as well as their time profiles. Comparison of measured and computed concentrations has also allowed an estimation of the degree of air entrainment.

OCIS codes: 300.6365, 000.1570, 350.5400.

1. Introduction

There has been considerable interest in the emission spectra from laser-induced plasmas. From an analytical point of view, the relative intensities of the various atomic and molecular features provide information with which to identify the material from which the plasma was created. The techniques of laser-induced breakdown spectroscopy (LIBS) [1–4] and laser ablation coupled plasma mass spectrometry [5] are based on this idea. Because little or no sample preparation is required, LIBS has been developed into a powerful method for the identification of many materials.

The relative intensities of the various atomic and molecular spectroscopic signatures depend upon the material entrained into the plasma and the physical and chemical processes occurring within the plasma. We are interested in developing a full chemical and physical model of the LIBS plume for various systems in order to understand in detail the various processes leading to the observable spectroscopic signatures. A full treatment of the processes occurring within the plume involves an understanding of both the plasma hydrodynamics and the relevant chemical and physical processes. In this work on LIBS of two representative organic compounds, we concentrate on the latter processes and use experimental observations of the plasma to constrain its temperature and electron density. We present a kinetic model to describe the neutral and ionic chemistry, as well as processes leading to the production and removal of the excited, emitting C/H/N/O atomic levels. In previous work, we carried out similar studies of LIBS of metallic lead in air and argon atmospheres [6,7], as well as LIBS of RDX in air [8]. In the present study, we compare the results of our kinetic modeling with experimentally determined relative LIBS emission intensities in order to test the ability of our model to describe the excited-state populations.

Several groups have developed models to explain the plasma formation and plume expansion dynamics, and representative studies are described here. Bogaerts and co-workers have considered the laser ablation of Cu and the plasma expansion in different background gases and in the double-pulse configuration

0003-6935/10/130C58-09$15.00/0

Report Documentation Page

Form Approved
OMB No. 0704-0188

1. REPORT DATE	2. REPORT TYPE	3. DATES COVERED
2010		**00-00-2010 to 00-00-2010**

4. TITLE AND SUBTITLE	5a. CONTRACT NUMBER
Kinetic model of C/H/N/O emissions in laser-induced breakdown spectroscopy of organic compounds	**W911NF-06-1-0446**
	5b. GRANT NUMBER
	5c. PROGRAM ELEMENT NUMBER
6. AUTHOR(S)	5d. PROJECT NUMBER
	5e. TASK NUMBER
	5f. WORK UNIT NUMBER

7. PERFORMING ORGANIZATION NAME(S) AND ADDRESS(ES)	8. PERFORMING ORGANIZATION REPORT NUMBER
Department of Chemistry,The Johns Hopkins University,Baltimore,MD,21218	**; 50351.27**
9. SPONSORING/MONITORING AGENCY NAME(S) AND ADDRESS(ES)	10. SPONSOR/MONITOR'S ACRONYM(S)
U.S. Army Research Office, P.O. Box 12211, Research Triangle Park, NC, 27709-2211	11. SPONSOR/MONITOR'S REPORT NUMBER(S) **50351.27**

12. DISTRIBUTION/AVAILABILITY STATEMENT
Approved for public release; distribution unlimited

13. SUPPLEMENTARY NOTES

14. ABSTRACT

15. SUBJECT TERMS

16. SECURITY CLASSIFICATION OF:			17. LIMITATION OF ABSTRACT	18. NUMBER OF PAGES	19a. NAME OF RESPONSIBLE PERSON
a. REPORT	b. ABSTRACT	c. THIS PAGE			
unclassified	**unclassified**	**unclassified**	**Same as Report (SAR)**	**9**	

[9,10]. Capitelli and co-workers have considered both equilibrium and nonequilibrium conditions in laser-induced plasmas through a time-dependent collisional–radiative model of the atomic excited-state populations and the electron energy distribution [11,12]. Vidal *et al.* [13] carried out a one-dimensional Lagrangian hydrodynamics calculation of the plasma expansion from ablation of aluminum in ambient air. Ashfold and co-workers have carried out 2-dimensional plasma and chemical modeling of a diamond deposition reactor and compared the results with experimental observations [14].

2. Kinetic Model

We have considerably extended the kinetic model previously developed [6] to describe air oxidation and ionization in the LIBS plume of lead in air. Our kinetic model includes reactions describing air oxidation and plasma chemistry, as well as the thermal decomposition of small organic compounds (those containing ≤4 carbon atoms). The rate constants were obtained from various databases and review articles [15–20], as well as a number of research papers.

A significant aspect of our kinetic model is the inclusion of the excited electronic states of H, C, N, and O atoms, which are required to describe the populations of the emitting, excited states of these elements. Table 1 lists the atomic states included in the model, as well as the relevant emission lines. We have included transitions in the VUV, which are not observed in LIBS spectra but which depopulate the lower levels of the observed LIBS lines. While not radiatively connected with the observed emission lines, the low-lying C, N, and O levels associated with the ground electron configurations are included since their concentrations can be significant and electron-impact excitation of these levels can populate the emitting levels.

We now consider the process populating and depleting the excited atomic electronic states. The excited states were assumed to be populated only by electron-impact excitation of the states associated with the ground atomic electron configuration. The temperature-dependent excitation rate constants for H and C were taken from the National Institute for Fusion Science atomic and molecular database [21], while the corresponding rate constants for N and O were derived from effective collision strengths computed by Tayal [22] and Zatsarinny and Tayal [23], respectively. Electron-impact de-excitation rate constants were computed by detailed balance. Heavy-particle excitation was not included in the model since this process occurs predominantly at keV energies [24]; similarly, production of excited states by electron-ion recombination was neglected. In addition to electron-impact de-excitation, radiative decay [25] and collisional electronic quenching by neutral species were included as processes depopulating excited atomic states. Unfortunately, electronic quenching rate constants are available only for stable collision partners at room temperature.

Table 1. Atomic Energy Levels Included in the Kinetic Model

Notation	Level	Energy (cm^{-1})	Emission Line (nm)[a]
Hydrogen			
H	$n = 1$	0	97.2, 102.6, 121.6 (L)
H*2	$n = 2$	82259	121.6 (U), 486, 656 (L)
H*3	$n = 3$	97492	102.6 (U), 656 (U)
H*4	$n = 4$	102824	97.2, 486 (U)
Carbon			
C	$2s^2 2p^2\ ^3P$	0	156.1, 165.7 (L)
C*2	$2s^2 2p^2\ ^1D$	10194	193.7 (L)
C*3	$2s^2 2p^2\ ^1S$	21648	247.9 (L)
C*4	$2s^2 2p 3s\ ^3P°$	60360	165.7 (U)
C*5	$2s^2 2p 3s\ ^1P°$	61982	193.7, 247.9 (U)
C*6	$2s 2p^3\ ^3D°$	64091	156.1 (U)
Nitrogen			
N	$2p^3\ ^4S°$	0	120.0, 113.4 (L)
N(2D)	$2p^3\ ^2D°$	19226	149.3 (L)
N(2P)	$2p^3\ ^2P°$	28840	174.3 (L)
N*4	$2p^2 3s\ ^4P$	83337	120.0 (U), (742–746), (818–821),(868–874) (L)
N*5	$2p^2 3s\ ^2P$	86192	149.3,174.3 (U)
N*6	$2s 2p^4\ ^4P$	88134	113.4 (U)
N*8[b]	$2p^2 3p\ ^4D°$	94839	(868–874) (U)
N*9	$2p^2 3p\ ^4P°$	95511	(818–821) (U)
N*10	$2p^2 3p\ ^4S°$	96752	(742–746) (U)
Oxygen			
O	$2p^4\ ^3P$	0	130.4 (L)
O(1D)	$2p^4\ ^1D$	15868	
O(1S)	$2p^4\ ^1S$	33793	
O*4	$3s\ ^5S°$	73768	777 (L)
O*5	$3s\ ^3S°$	76794	130.4 (U), 845 (L)
O*6	$3p\ ^5P$	86626	777 (U)
O*7	$3p\ ^3P$	88631	845 (U)

[a]U or L denotes that this level is the upper or lower level, respectively, of the emission line.

[b]N*7 denotes the $2p^2 3p\ ^2S°$ state, which lies at 93582 cm^{-1} but which was not included in the kinetic model.

While CN and C_2 molecular emission is usually observed in LIBS of organic compounds [26,27], as is the case in the present experiments, the available data on electron-impact excitation of the excited molecular states are lacking, and we did not include these states in our model. Since our organic compounds were prepared as residues on Al foil (see Section 3), emission of Al lines, due to ablation of the substrate, was also observed. Sufficient literature data are available to include several Al species in our model [Al, Al*4*S*, Al^+, AlO, AlH] in order to allow us to interpret the Al 394–396 nm [$4s^2 S_{1/2} \rightarrow 3p^2 P°_{1/2,3/2}$] line intensities relative to those of the light atoms. The energy-dependent electron-impact excitation cross section to the 4*S* state was taken from Smirnov [28]. The early stage of Al oxidation was taken into account by inclusion of the species AlO and AlH.

The Chemkin package [29] was employed to solve the differential equations governing the time-dependent concentrations. We have ignored spatial variations of the concentrations and have assumed a homogeneous closed reactor model. To match the required format of the input data, the temperature

dependence of the rate constants of the included processes were fitted to the functional form $k = AT^n \exp(-E_a/RT)$, where T is the temperature (in degrees Kelvin) and A, n, and E_a are fitted parameters. A total of 134 species (including the atomic states listed in Table 1) and 1501 processes (with forward and reverse processes listed separately) were included in the kinetic model. A list of the processes and the kinetic parameters, as well as the sources for the rate constants, can be obtained from one of the authors (PJD). In addition to the matrix of rate constants, integration of the rate constants requires specification of the initial concentrations, which are determined by the laser–matter interaction, and the temperature temporal profile. As described in Section 4, we make various assumptions about the initial concentrations and derive an estimated temperature profile from experimental data. In all cases, we assumed a constant pressure of 1 atm in the simulations.

3. Experimental Apparatus

The apparatus employed for measurement of LIBS intensities is similar to that used in previous LIBS investigations in our laboratory [27,30], and a brief description is provided here. Single pulses of 355 nm radiation (tripled Nd:YAG fundamental from a Continuum Powerlite 8000, ~7 ns pulse width, 10 Hz repetition rate) were passed through a mechanical shutter and focused with a 50 mm focal length lens onto the sample, which was mounted on a motorized translation stage. A fresh area was irradiated on each laser shot in ambient air. Emission (200–860 nm) from the LIBS plasma was focused with a pair of 30° off-axis parabolic mirrors (focal length 25.4 mm) onto a UV-transmitting optical fiber (50 μm core). The output of the fiber was transmitted to an echelle spectrometer (Andor Mechelle 5000) equipped with a gated, intensified charge coupled device (ICCD) (Andor DH734-18-03). The ICCD delay and gate width were controlled by a digital delay generator (Stanford Research Systems DG535). The gate width was fixed at 100 ns, and delays from 20 ns to 3 μs were employed. The wavelength-dependent sensitivity of the optical fiber/spectrometer/ICCD combination was determined by recording spectra of calibrated deuterium and tungsten-halogen lamps, and the spectra were corrected for the varying sensitivity. Atomic line intensities were computed by determining the area under the line profile above any background.

The two organic compounds investigated, anthracene and 2,4-dinitrotoluene (Sigma-Aldrich), were prepared as residues on aluminum foil substrates. For each compound, a 10 μl aliquot of a nearly saturated solution in methanol was delivered to the substrate surface, and the solution was allowed to dry in the hood. The resulting spot size was measured to determine the average surface coverage, which was ~25 and 40 $\mu g/cm^2$ for anthracene and 2,4-dinitrotoluene, respectively.

4. Results and Discussion

A. Bare Al Foil

We first consider LIBS of bare Al foil in ambient air in order to investigate the relative concentrations of the light atoms and the Al atom in excited, emitting states. We recorded LIBS spectra with the detector gate delay stepped in increments of 100 ns. The laser pulse energy was 20 mJ for these measurements. Figure 1 displays the Al 394–396 nm lines at several detector gate delays. It can be seen that the lines are quite broad at short delays and the widths decrease with increasing gate delay. The width of the lines is a result of Stark broadening due to the high initial electron density. It can be seen in Figs. 1(b)–1(d) that at longer delays there is self-absorption of the lines, due to the presence of Al atoms in the cooler parts of the plasma. It is also evident that the lines are Stark shifted, as well as broadened.

The wings of the line profiles were fitted to a Voigt function in order to determine the Stark width as a function of time. The fitted widths were employed to estimate the electron density, using literature data [31,32] for the linear Stark broadening parameter of the 394 nm line. The derived electron density as a function of time is presented in Fig. 2(b). It can be seen that the electron density at the shortest delay is estimated to be $\sim 3 \times 10^{18}$ electrons cm^{-3}. It should be noted that this electron density is approximately an order of magnitude greater than the density range at which the Stark parameters were measured, and hence our derived densities could have a systematic error.

It is also of interest to estimate the plasma temperature as a function of time, since this is important input for our kinetic modeling, as discussed above. We have utilized the ratio of the intensities of the Al 394.40 and 308.22 nm lines and the assumption of local thermodynamic equilibrium to derive the temperature as a function of time. In this analysis, the line intensities were computed as areas of Voigt profiles fitted to the wings of the lines, as both lines were subject to self-absorption (see Fig. 1). Figure 2(a) presents the derived temperature as a function of time. It can be seen that the temperature at the shortest delay is ~18,000 K and drops to ~10,000 K by 3 μs. These values were least squares fitted to an exponential decay plus a constant term in order to have a smooth temperature profile as input for the kinetic simulations. The scatter of the points about the fitted line gives an indication of the precision of this temperature measurement. It is certainly likely that the plasma at the shortest delays is not in thermodynamic equilibrium; however, this is the simplest model for use for input in the kinetic simulations.

Figure 3 presents the observed time dependence of the relative concentrations of the excited, emitting states of the light atoms and Al. These concentrations were determined from the areas of the emission lines and the known [25] radiative decay rates; the line intensity is proportional to the excited-state

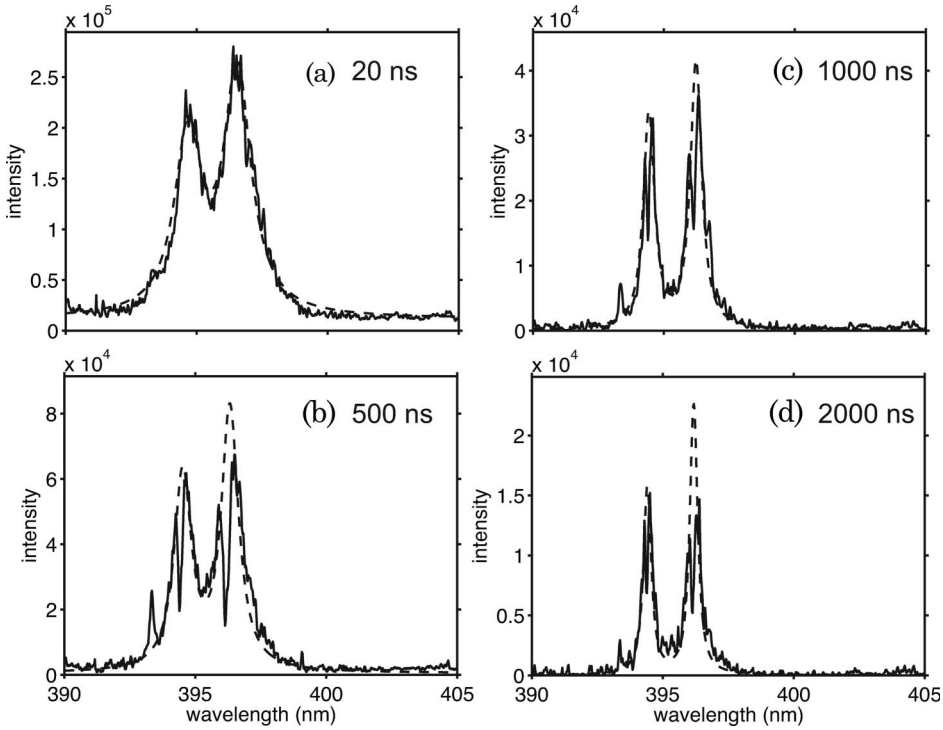

Fig. 1. Spectra of the Al 394–396 nm lines in LIBS of bare Al foil at detector gate delays of (a) 20 ns, (b) 500 ns, (c) 1000 ns, and (d) 2000 ns, with a gate width of 100 ns. The dotted lines represent Voigt profile fits to the wings of the lines. The 355 nm laser energy was 20 mJ per pulse.

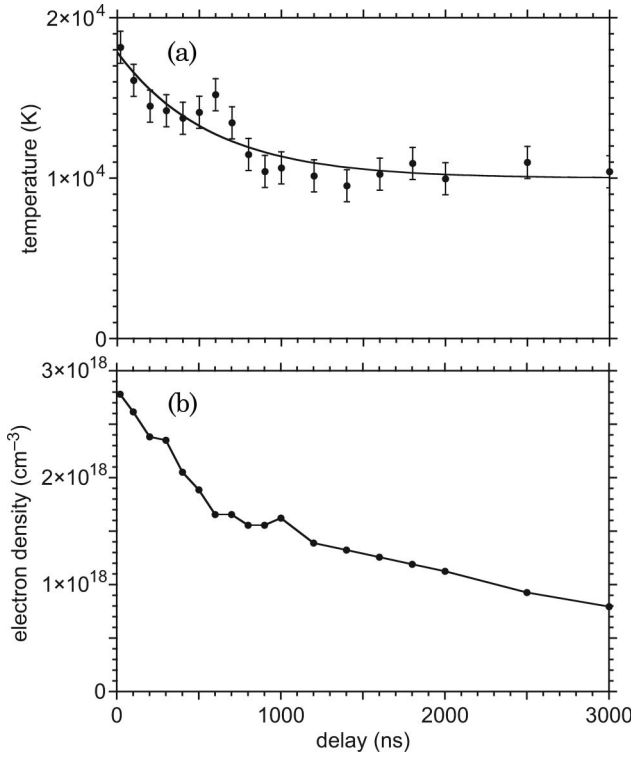

Fig. 2. (a) Plasma temperature and (b) electron density as a function of time after the 355 nm laser pulse (20 mJ) for LIBS of bare Al foil. The former was derived from the relative intensities of the Al 394.40 and 308.22 nm lines, while the latter was obtained from the Stark broadening of the 394.40 nm line (see text).

concentration multiplied by the radiative decay rate. We see that the concentrations of the excited N and O states are comparable in magnitude and have a similar time dependence. The initial concentration of the Al*4*S* state is somewhat greater, and the concentration of this state decays more slowly with time than the concentrations of the N and O states.

In order to interpret the observed excited-state concentrations, we have carried out kinetic simulations of the time-dependent species concentrations with methods described in Section 2. The temperature

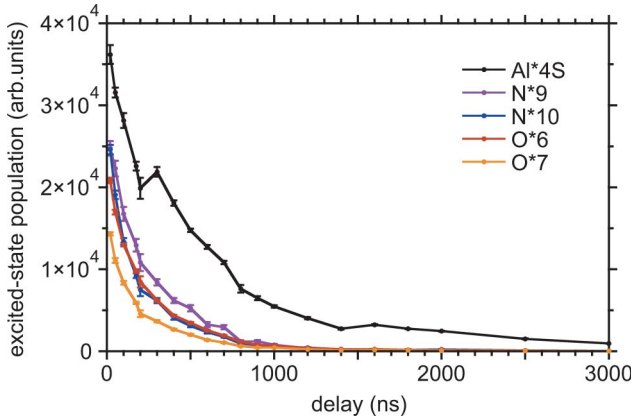

Fig. 3. (Color online) Relative populations of the Al*4*S*, N*9, N*10, O*6, and O*7 levels (in the notation of Table 1) determined from the measured intensities (corrected for the wavelength-dependent detection sensitivity) of atomic emission lines for the 355 nm laser irradiation (pulse energy 20 mJ) of bare Al foil in ambient air.

profile in these simulations was taken from the fit [smooth line in Fig. 2(a)] to the temperatures estimated from the Al atomic line ratios. As discussed in Section 2, one critical assumption in this modeling is the species concentrations after the laser pulse. We must also make assumptions as to the entrainment of the ablated Al and the ambient air into the LIBS plume. We have carried out simulations for various Al : air mole ratios in the plasma and find that our observed ratio of the Al*4*S* concentration to that of the excited N and O states is consistent with a very small Al : air mole ratio in the plasma.

We present in Fig. 4 computed time-dependent concentrations of the excited, emitting states for an assumed Al : air mole ratio of 0.1 and various assumptions for the initial species concentrations. In all cases, the computed Al*4*S* concentration is several orders of magnitude higher than those of the N and O states. In large part, this is due to the much larger rate constant for electron-impact excitation of the Al*4*S* state than those for the excited, emitting N and O states; the difference in the magnitudes of the rate constants is due to the lower Al*4*S* excitation energy.

It can be seen in Fig. 4 that the excited-state concentrations reach their maximum values at greatly different times for the various assumed initial concentrations. For assumed simple heating [Fig. 4(a)] the maximum N and O concentrations are reached ~300 ns after the laser pulse. In this case, the Al*4*S* concentration is computed to increase slightly after this induction period. By contrast, the maximum concentrations are reached ~100 ns after the laser pulse when complete atomization is assumed [Fig. 4(b)]. We see a similar concentration temporal profile when 10% ionization of Al is additionally assumed; the relatively small amounts of ions and electrons with this assumption do not significantly affect the computed concentrations. The computed concentrations with the assumption of complete atomization and 10% ionization of N are seen in Fig. 4(d) to lead to computed excited N and O atom time-dependent concentrations in reasonable agreement with experiment. In this case, the excited-state concentrations rise rapidly after the laser pulse on the time scale of the plot and decay with a rate similar to that seen in the experimentally determined excited-state concentrations (Fig. 3). Additionally, the calculations reproduce the observed much slower decay of the Al*4*S* state.

B. Anthracene

We chose anthracene ($C_{14}H_{10}$) as one of the organic compounds for study since the relative intensities of the N and O lines are a good measure of the degree of air entrainment for this hydrocarbon. Figure 5(a) presents the determined time dependence of the relative concentrations of the excited, emitting states of the light atoms and Al for LIBS of residues of anthracene on Al foil. A laser pulse energy of 20 mJ was employed. The concentrations and time dependence of the excited C, N, and O states are seen to be similar. The concentration of the H*3 state is similar to

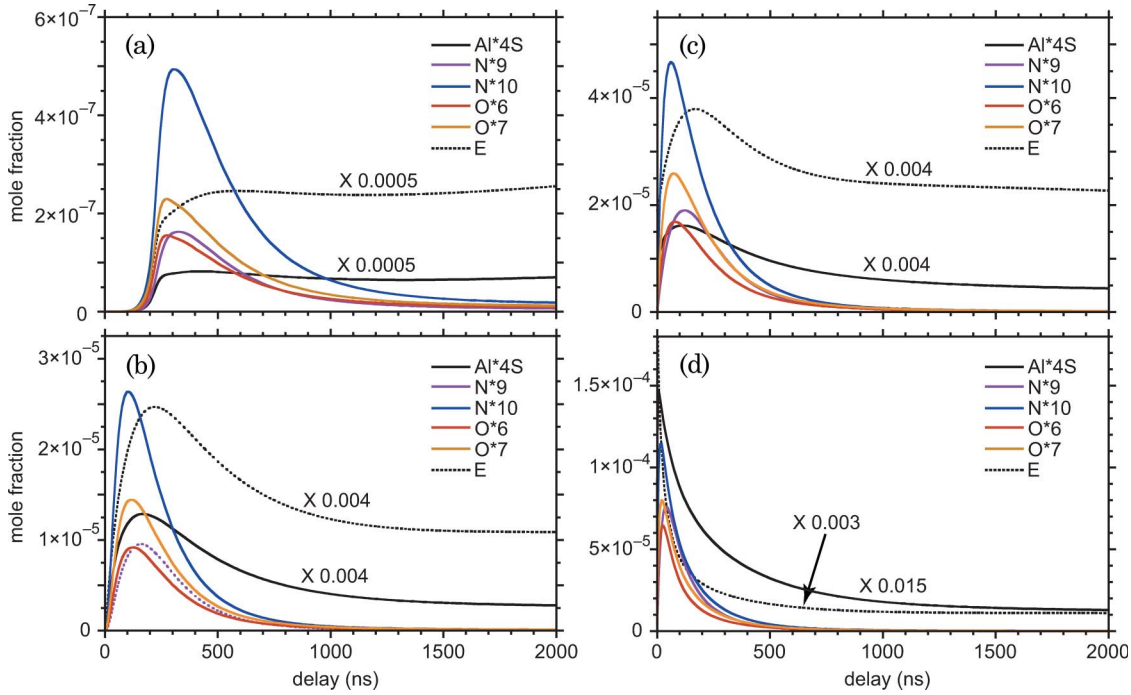

Fig. 4. (Color online) Plots of the time-dependent concentrations of the excited, emitting atomic levels (in the notation of Table 1) for an Al–air mixture (Al : air mole ratio 0.1), computed with the kinetic model described in Section 2 and the temperature plotted in Fig. 2(a). The assumed initial conditions and species mole ratios were as follows: (a) simple heating [Al, 1; N_2, 7; O_2, 3], (b) complete atomization [Al, 1; N, 14; O, 6], (c) atomization and 10% ionization of Al [Al, 0.9; Al^+, 0.1; E, 0.1; N, 14; O, 6], (d) atomization and 10% ionization of N [Al, 1; N, 12.6; N^+, 1.4; E, 1.4; O, 6]. The electron and Al*4*S* concentrations are scaled as indicated in the panels.

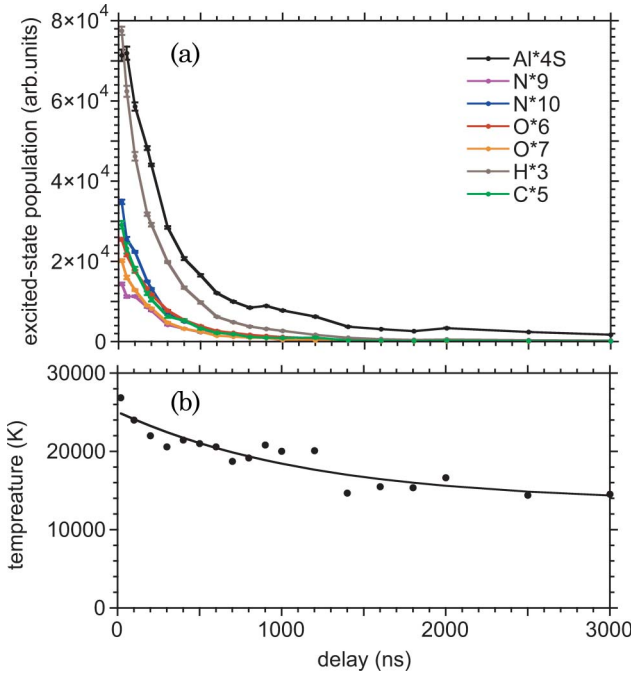

Fig. 5. (Color online) (a) Relative populations of the excited, emitting levels (in the notation of Table 1) determined from the measured intensities (corrected for the wavelength-dependent detection sensitivity) of atomic emission lines for the 355 nm laser irradiation (pulse energy 20 mJ) of amthracene residue on Al foil in ambient air. (b) Plasma temperature, derived from the relative intensities of the Al 394.40 and 308.22 nm lines, as a function of time after the 355 nm laser pulse (20 mJ) for LIBS of anthracene residue on Al foil.

that of Al*4*S* at short delays but decreases more rapidly. As in the case of LIBS of bare Al foil, the Al*4*S* [Fig. 3], the Al*4*S* concentration persists for a significantly longer time than do the concentrations of the light atoms. We also see that the Al*4*S* concentration extends to longer delays than the excited-state concentrations of the lighter atoms, as was also observed in Fig. 3 for LIBS of bare Al foil in ambient air.

Figure 5(b) displays the temporal dependence of the plasma temperature, estimated from the ratio of the Al 394.40 and 308.22 nm lines, as determined by the procedure described in Subsection 4.A. The initial temperature was found to be somewhat higher than in the case of LIBS of bare Al foil [see Fig. 2(a)].

We have carried out kinetic simulations of anthracene–air mixtures with the methods described in Section 2. We have not included Al in the reaction mixture since the Al mole fraction required to model the observed Al*4*S* relative concentrations was found in Subsection 4.A to be much too low to affect the chemistry of the light atoms. The temperature profile in the simulations was taken from the fit [smooth line in Fig. 5(b)] to the temperatures estimated from the Al atomic line ratios.

As discussed above, we must also make an assumption about the initial concentrations, immediately after the laser pulse. In the case of LIBS of bare Al foil [Subsection 4.A], we found that prompt formation of the excited, emitting states was computed only if complete atomization and partial ionization was assumed. We have employed this assumption in our kinetic simulations for both anthracene and 2,4-dinitrotoluene [discussed in Subsection 4.C]. In the case of anthracene, we assume 10% ionization of the C atoms.

Figure 6 presents computed time-dependent concentrations of the excited, emitting light atoms for two assumed anthracene–air mole ratios (1:5 and 1:10). In both cases, the H*3 state is computed to have the highest concentration of the emitting states. The second most populated state is predicted to be the C*5 state. The concentrations of the emitting N and O states are lower and are found to scale approximately linearly with the air–anthracene mole ratio. Also plotted in both panels of Fig. 6 is the computed electron density, which is estimated to be several orders of magnitude larger than the excited-state atom concentrations. We also see that the electron density is computed initially to increase slightly and then decay much more slowly than the concentrations of the emitting states of the light atoms.

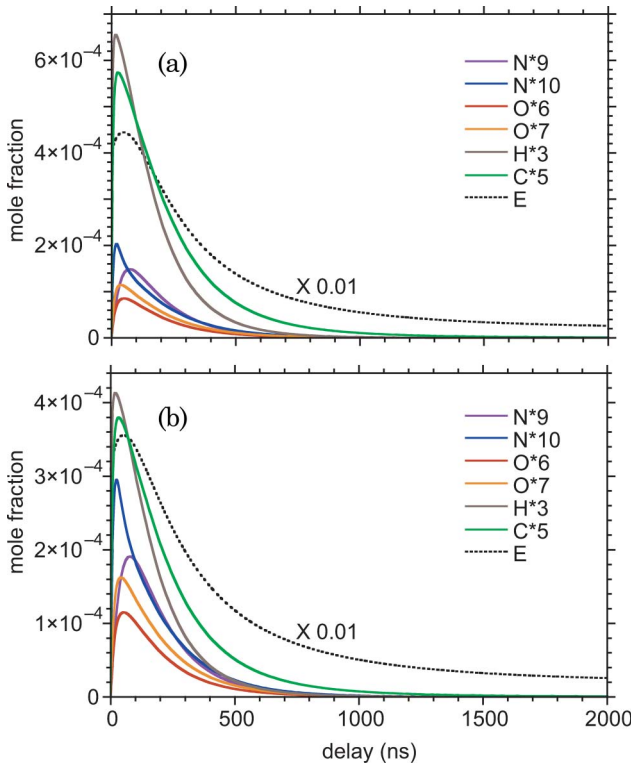

Fig. 6. (Color online) Plots of the time-dependent concentrations of the excited, emitting atomic levels (in the notation of Table 1) for an anthracene–air mixture, computed with the kinetic model described in Section 2 and the temperature plotted in Fig. 5(a) . The assumed initial conditions and species mole ratios were as follows: (a) anthracene–air mixture at a 1:5 mole ratio, with assumed complete atomization and 10% ionization of C [C, 12.6; C^+, 1.4; E, 1.4; H, 10; N, 7; O, 3] and (b) anthracene–air mixture at a 1:10 mole ratio, with assumed complete atomization and 10% ionization of C [C, 12.6; C^+, 1.4; E, 1.4; H,10; N, 14; O, 6]. The electron concentration is scaled as indicated in the panels.

In simulations with other temperature profiles, we found that the relative concentration of the C*5 state is somewhat sensitive to the plasma temperature. By contrast, the relative concentrations of the H, N, and O excited states do not seem to depend significantly upon the plasma temperature. The sensitivity of the C*5 state concentration is due to the low ionization potential of C and the relatively low excitation energy of the C*5 state, as compared to the corresponding quantities for the other atoms.

Comparison of the computed concentrations in Fig. 6 and those measured experimentally [see Fig. 5(a)] shows that a kinetic simulation with an assumed anthracene–air mole ratio of 5:1 to 10:1 provides a reasonable representation of the experimental results. The H*3 concentration is found to be the largest, as was observed experimentally. The computed excited-state concentrations decay at a rate similar to what was observed experimentally. The major difference between the experimental determined and computed concentrations is the relative concentration of the C*5 state, which was computed to be comparable to that of the H*3 state, while the C*5 to H*3 concentration ratio was determined experimentally to be approximately 0.5 at short delays. It is possible that we have underestimated the uncertainty in experimentally determined the C*5 relative concentration. This state emits in the UV, far from the wavelengths of the other emission lines, which occur in the red. The sensitivity of our detection system is much less in the UV, by a factor of ~40 at 248 nm (wavelength of the C*5 line), than in the red, at 656 nm (wavelength of the H*3 line).

C. 2,4-Dinitrotoluene

Our second organic sample was chosen to be 2,4-dinitrotoluene, which has a large N and O mole fraction, similar to that in many explosives. Figure 7(a) presents the determined time dependence of the relative concentrations of the excited, emitting states of the light atoms and Al for LIBS of residues of the compound on Al foil. A laser pulse energy of 10 mJ was employed. For the light atoms, the determined concentrations and time profiles of the emitting states of C, N, and O are similar, while the H*3 concentration is approximately a factor of 2 larger. As we observed for LIBS of bare Al foil and of anthracene residue, the Al*4*S* concentration decays much more slowly and persists for longer delay times.

Figure 7(b) presents the temporal dependence of the plasma temperature, determined from the ratio of the Al 394.40 and 308.22 nm lines. The temperature was found to be somewhat lower than that found for LIBS of anthracene. It should be noted that the laser pulse energy was 10 mJ, lower than that employed for LIBS of anthracene (20 mJ).

Kinetic simulations of 2,4-dinitrotoluene–air mixtures, following the procedures described in Section 2, were carried out. As was done for simulations of anthracene–air mixtures, Al was not included in the reaction mixture. The temperature profile in

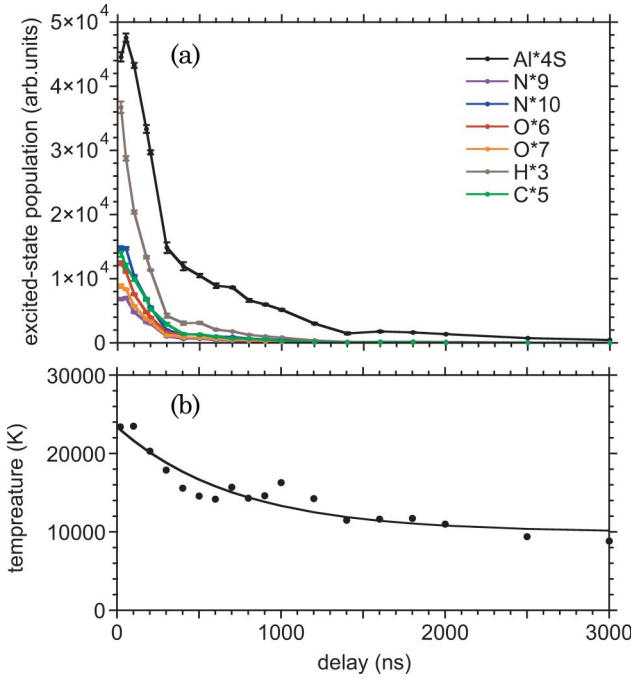

Fig. 7. (Color online) (a) Relative populations of the excited, emitting levels (in the notation of Table 1) determined from the measured intensities (corrected for the wavelength-dependent detection sensitivity) of atomic emission lines for the 355 nm laser irradiation (pulse energy 10 mJ) of 2,4-dinitrotoluene residue on Al foil in ambient air. (b) Plasma temperature, derived from the relative intensities of the Al 394.40 and 308.22 nm lines, as a function of time after the 355 nm laser pulse (10 mJ) for LIBS of 2,4-dintirotoluene residue on Al foil.

the simulations was taken from the fit [smooth line in Fig. 7(b)] to the temperatures estimated from the Al atomic line ratios. As in Subsection 4.B, we took complete atomization and partial ionization (see the caption of Fig. 8 for details) as our assumption for the initial concentrations. With this assumption, prompt formation of the excited, emitting state was found in the simulations.

Figure 8 presents computed time-dependent concentrations of the excited, emitting light atoms for pure 2,4-dinitrotoluene and an assumed 1:2.5 2,4-dinitrotoluene–air mole ratio. The H*3 state is computed to have the highest concentration in both simulations, while the second most populated state is predicted to be the C*5 state. In the simulation of pure 2,4-dinitroluene, the concentrations of the emitting N and O states are more than a factor of 2 lower than that of H*3. We also see in this case that the O atom concentrations are predicted to be approximately a factor of 2 larger than those of the N atom states. This is consistent with the larger mole fraction of O than N in the pure compound. The simulations of the 2,4-dinitrotoluene–air mixture yield higher relative concentrations of the excited N and O atom states, as expected. In this case, the excited N and O state concentrations are comparable. This is a result of the greatly different N to O mole ratio in air than in 2,4-dinitrotoluene. Also plotted in Fig. 8 is the computed electron density. As in Fig. 6, the

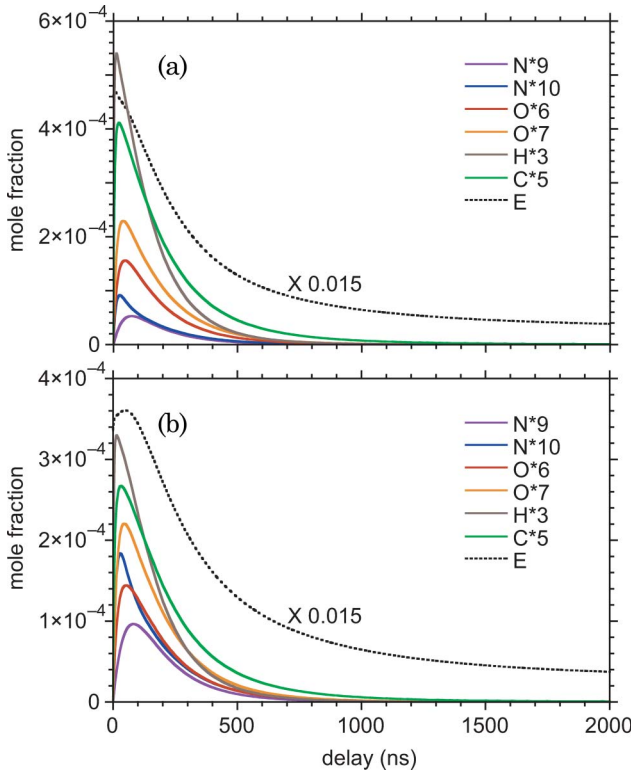

Fig. 8. (Color online) Plots of the time-dependent concentrations of the excited, emitting atomic levels (in the notation of Table 1) for a 2,4-dinitrotoluene–air mixture, computed with the kinetic model described in Section 2 and the temperature plotted in Fig. 7(b). The assumed initial conditions and species mole ratios were as follows: (a) pure 2,4-dinitrotoluene, with assumed complete atomization and 10% ionization of C [C, 6.3; C^+, 0.7; E, 0.7; H, 6; N, 2; O, 4], and (b) 2,4-dinitrotoluene–air mixture at a 1:2.5 mole ratio, with assumed complete atomization and 10% ionization of N [C, 7; H, 6; N, 4.95; N^+, 0.55; E, 0.55; O, 6]. The electron concentration is scaled as indicated in the panels.

electron density is computed initially to increase and then to decay more slowly than the excited-state concentrations.

The excited-state concentrations computed with an assumed 2,4-dinitrotoluene–air mole ratio of 1:2.5 [Fig. 8(a)] provide a reasonable representation of the experimentally measured excited-state concentrations plotted in Fig. 7(a). While the molecule-to-air mole ratio in the optimum simulations was a factor of ~2 different for anthracene and 2.4-dinitrotoluene, the atom mole ratios are similar. As with the comparison of observed and computed concentrations for anthracene [Figs. 5(a) and 6(a), respectively], the major difference is the relative concentration of the C*5 state, which is computed to be lower than is measured experimentally. This discrepancy could be the result of the poor UV sensitivity of our detection system, and the consequent error in correcting the raw intensities.

5. Conclusion

In this paper, we have presented a kinetic model of the physical and chemical processes determining the concentrations of the excited, emitting atomic states responsible for the atomic emission signatures in LIBS spectra. To provide a complete picture of the LIBS process, this model would need to be coupled with a theoretical description for the ablation and the hydrodynamics of the plasma plume. It is also known that particles are often ejected from surfaces in laser ablation, and this process would need to be included in a full description of the LIBS process. In this work, the temperature and electron density as a function of time were estimated from ratios of atomic line intensities and Stark broadening, respectively. It was also necessary to assume the initial concentrations of the various species, in order to describe the effect of the laser interaction on the ablated material and the ambient atmosphere.

We have compared the predictions of this model with recorded LIBS spectra of several samples, including bare Al foil and two organic compounds, anthracene and 2,4-dinitrotoluene, in ambient air. Our kinetic simulations predict excited-state concentrations and their time profiles which are in reasonable agreement with relative concentrations derived from the experimentally measured line intensities in the LIBS spectra. We also were able to obtain an estimate of the degree of air entrainment into the plasma plume.

The modeling includes several components. The first is the matrix of rate constants and their dependence upon temperature, and in some case their pressure dependence. Experimentally determined reaction rate constants have generally been determined for temperatures ≤3000 K, and these rate constants need to be extrapolated up to plasma temperatures. Fortunately, we would expect chemical compounds to be completely atomized at these high temperatures. A more uncertain component of the model is the need to assume initial concentrations to describe the dissociation and ionization caused by the laser–matter interaction. It is thus gratifying that our kinetic modeling does yield computed relative concentrations in reasonable agreement with the experimentally determined values. Measurement of absolute concentrations would provide an even more stringent test of the kinetic model; unfortunately, such an experiment is fraught with significant likely systematic errors.

This research has been supported by the U.S. Army Research Office under the Multidisciplinary University Research Initiative project W911NF-06-1-0446.

References

1. L. J. Radziemski and D. A. Cremers, eds., *Laser-Induced Plasmas and Applications* (Dekker, 1989).
2. A. W. Miziolek, V. Palleschi, and I. Schechter, eds., *Laser-Induced Breakdown Spectroscopy (LIBS): Fundamentals and Applications* (Cambridge U. Press, 2006).
3. D. A. Cremers and L. J. Radziemski, *Handbook of Laser-Induced Breakdown Spectroscopy* (Wiley, 2006).
4. J. P. Singh and S. N. Thakur, eds., *Laser-Induced Breakdown Spectroscopy* (Elsevier, 2007).

5. J. Gonzalez, C. Liu, J. Yoo, X. Mao, and R. E. Russo, "Double-pulse laser ablation inductively coupled plasma mass spectrometry," Spectrochim. Acta Part B **60**, 27–31 (2005).
6. V. I. Babushok, F. C. DeLucia, Jr., P. J. Dagdigian, M. J. Nusca, and A. W. Miziolek, "Kinetic modeling of the laser-induced breakdown spectroscopy plume from metallic lead," Appl. Opt. **42**, 5947–5962 (2003).
7. V. I. Babushok, F. C. DeLucia, Jr., P. J. Dagdigian, and A. W. Miziolek, "Experimental and kinetic modeling study of the laser-induced breakdown spectroscopy plume from metallic lead in argon," Spectrochim. Acta Part B **60**, 926–934 (2005).
8. V. I. Babushok, F. C. DeLucia, Jr., P. J. Dagdigian, J. L. Gottfried, C. A. Munson, M. J. Nusca, and A. W. Miziolek, "Kinetic modeling study of the laser-induced plasma plume of the explosive cyclotrimethylenetrinitramine" (RDX)," Spectrochim. Acta Part B **62**, 1321–1328 (2007).
9. A. Bogaerts, Z. Chen, and D. Bleiner, "Laser ablation of copper in different background gases: comparative study by numerical modeling and experiments," J. Anal. At. Spectrom. **21**, 384–395 (2006).
10. A. Bogaerts, Z. Chen, and D. Autrique, "Double pulse laser ablation and laser induced breakdown spectroscopy: a modeling investigation," Spectrochim. Acta Part B **63**, 746–754 (2008).
11. A. Casavola, G. Colonna, A. De Giacomo, and M. Capitelli, "Laser ablation of titanium metallic targets: comparison between theory and experiment," J. Thermophys. Heat Transf. **17**, 225–231 (2003).
12. M. Capitelli, A. Casavola, G. Colonna, and A. De Giacomo, "Laser-induced plasma expansion: theoretical and experimental aspects," Spectrochim. Acta Part B **59**, 271–289 (2004).
13. F. Vidal, S. Laville, T. W. Johnston, O. Barthélemy, M. Chaker, B. Le Drogoff, J. Margot, and M. Sabsabi, "Numerical simulations of ultrashort laser pulse ablation and plasma expansion in ambient air," Spectrochim. Acta B **56**, 973–986 (2001).
14. C. J. Rennick, R. Engeln, J. A. Smith, A. J. Orr-Ewing, and M. N. R. Ashfold, "Measurement and modeling of a diamond deposition reactor: hydrogen atom and electron number densities in an Ar/H_2 arc jet discharge," J. Appl. Phys. **97**, 113306 (2005).
15. NIST Chemical Kinetics Database <http://kinetics.nist.gov/kinetics/index.jsp>.
16. D. L. Baulch, D. D. Drysdale, J. Duxbury, and S. J. Grant, *Evaluated Kinetic Data for High Temperature Reactions. Volume 3. Homogeneous Gas Phase Reactions of the* O_2—O_3 *System, the* CO—O_2—H_2 *System, and of Sulphur-Containing Species* (Butterworths, 1976).
17. D. L. Baulch, C. J. Cobos, R. A. Cox, P. Frank, G. Hayman, Th. Just, J. A. Kerr, T. Murrells, M. J. Pilling, J. Troe, R. W. Walker, and J. Warnatz, "Evaluated kinetic data for combustion modelling. Supplement I," J. Phys. Chem. Ref. Data **23**, 847–1033 (1994).
18. C. Park, J. T. Howe, R. J. Jaffe, and G. V. Candler, "Review of chemical-kinetic problems of future NASA missions, II: Mars entries," J. Thermophys. Heat Transf. **8**, 9–23 (1994).
19. W. L. Morgan, "Electron collision data for plasma modeling," Adv. At. Mol. Opt. Phys. **43**, 79–110 (2000).
20. GRI-Mech combustion model <http://www.me.berkeley.edu/gri-mech/>.
21. Atomic & Molecular Numerical Databases National Institute for Fusion Science-Japan <https://dbshino.nifs.ac.jp/>.
22. S. S. Tayal, "Effective collision strengths for electron impact excitation of N I," At. Data Nucl. Tables **76**, 191–212 (2000).
23. O. Zatsarinny and S. S. Tayal, "Electron collision excitation rates for O I using the *B*-spline *R*-matrix approach," Astrophys. J. Suppl. Ser. **148**, 575–582 (2003).
24. D. Detleffsen, M. Anton, A. Werner, and K.-H. Schartner, "Excitation of atomic hydrogen by protons and multiply charges ions at intermediate velocities," J. Phys. B: At. Mol. Opt. Phys. **27**, 4195–4213 (1994).
25. NIST Atomic Spectra Database, version 3 <http://physics.nist.gov/PhysRefData/ASD>.
26. A. Portnov, S. Rosenwaks, and I. Bar, "Emission following laser-induced breakdown spectroscopy of organic compounds in ambient air," Appl. Opt. **42**, 2835–2842 (2003).
27. D. M. Wong and P. J. Dagdigian, "Comparison of laser-induced breakdown spectra of organic compounds with irradiation at 1.5 and 1.064 μm," Appl. Opt. **47**, G149–G157 (2008).
28. Yu. M. Smirnov, "Cross sections for aluminum atom excitation by electron impact," Opt. Spectrosc. **82**, 200–204 (1997).
29. Chemkin-PRO, (Reaction Design, San Diego, California, USA, 2008) <http://www.reactiondesign.com>.
30. A. Khachatrian and P. J. Dagdigian, "Laser-induced breakdown spectroscopy with laser irradiation on mid-infrared hydride stretch transitions: polystyrene," Appl. Phys. B **97**, 243–248 (2009).
31. C. Fleurier, S. Sahal-Bréchot, and J. Chapelle, "Stark profiles of Al I and Al II lines," J. Phys. B: At. Mol. Phys. **10**, 3435–3441 (1977).
32. N. Konjevic and M. S. Dimitrijevic, "Experimental Stark widths and shifts for spectral lines of neutral atoms: a critical veview of selected data for the period 1976 to 1982," J. Phys. Chem. Ref. Data **13**, 619–647 (1984).